Single-Step Selective Oxidation of Methane by Iron-Oxo Species in the Metal-Organic Framework MFU-4l

Patrick Melix,[a,b,*] Randall Q. Snurr[a,*]

a Department of Chemical and Biological Engineering, Northwestern University, 2145 Sheridan Road, Evanston, Illinois 60208, United States

b Universität Leipzig, Wilhelm-Ostwald-Institut für Physikalische und Theoretische Chemie, Linnéstraße 2, 04103 Leipzig, Germany

Abstract

The direct and selective conversion of methane to methanol can be considered a holy grail for catalysis research. In this work, we study a metal-organic framework known as MFU-4l, modified by design to include highly reactive iron-oxo species for the catalytic C-H bond activation of methane. We investigate the oxidation of methane and the further potential oxidation of the product methanol using N_2O as an oxygen source and map the potential energy landscape of these reactions using density functional theory calculations. We show that the highest energy barrier encountered during the methane oxidation process is not the C-H bond breaking, but the activation of the iron center by N_2O. Furthermore, the potential energy landscape for the C-H bond activation exhibits a large, high-energy plateau region instead of a sharp transition state, thus differing from the traditional radical rebound mechanism. This insight offers interesting potential routes to enhance the catalytic activity of the catalyst, to hinder unwanted deactivation pathways, and to reduce the activity towards the over-oxidation of the product.

Keywords

MOF, MFU-4l, Methane, Oxidation, Methanol, Catalysis, DFT

Introduction

Natural gas consists mainly of methane,[1] an important resource that can unfortunately have a significant impact on our climate if released into the atmosphere.[2] Methane can, however, be used to produce another important base chemical: methanol. Methanol is currently synthesized from methane through the creation of syngas, a thermodynamically inefficient process, as it requires high temperatures and pressures to overcome the reaction energy of +206 kJ/mol in steam reforming.[3,4] Due to the need for intermediate syngas creation, the on-site usage of methane at smaller and remote sources of methane is greatly hindered, and the methane at such remote sites is often simply flared, as its transport to other locations is not easily achieved.[4,5] Methanol, however, can be stored and transported with much less effort, as it is a liquid under ambient conditions. A direct and selective pathway from methane to methanol, usable at small and large scales, would therefore greatly decrease the environmental impact of remote methane sources, as well as methanol-derived substances and methanol-based fuels. A key challenge is achieving high selectivity in the direct methane to methanol reaction. Burning methane is easy, stopping at methanol is not.[6,7]

Recently, many advances in the field of methane activation have been made. Inspired by enzymes, many biomimetic, homogeneous catalysts have been designed[8–11] to achieve the goal of high selectivity combined with high yield. However, industrially, heterogeneous catalysts provide many advantages. From a chemical perspective, metal-organic frameworks (MOFs) offer an intriguing possibility to create catalysts that combine the best features of homogeneous catalysts, namely their atomically precise structures[12,13] and vast possibilities for tuning,[14,15] with the advantages of a solid material. MOFs are also an ideal platform to understand reaction mechanisms in detail and then propose new design strategies for further investigation. Two important design goals for a MOF catalyst for the selective conversion of methane to methanol are suggested by economics and prior work: 1) the catalyst should be active under mild conditions[16] and 2) the obtained methanol should be protected to prevent overoxidation.[6] Metal-oxo centers are active species for the activation of the C-H bond of methane and other alkanes[10,17–22] and can be designed into a variety of MOF structures. Also, the secondary interactions[23,24] and geometric effects of the host system (sometimes called second-sphere effects) can be exploited to control reaction mechanisms in nanoporous materials as recently shown by Snyder *et al*.[25] The mobility of the CH_3 radical involved in many mechanisms for methane activation proved to be a key factor in the activity of zeolites incorporating metal-oxo centers, which have already been shown to be active for continuous methane oxidation using N_2O and H_2O.[26]

In MOFs, iron-oxo centers (Fe=O) have been successfully incorporated into the Fe_2(dobdc) family (Fe-MOF-74, dobdc^{4-}=2,5-dioxido-1,4-benzenedicarboxylate) and have been shown to be catalytically active towards C-H bond cleavage in experiment and theory.[27,28] For the case of ethane to ethanol conversion, this MOF exhibited a high selectivity due to the strong binding of the product to the open metal sites, resulting, however, in a low yield[27,29] in both flow-through and batch operation modes as the reactive sites become blocked by the strongly bound product. Many other systems incorporating metal-oxo centers have since then been investigated for the oxidation of methane by computational means.[30–34] Also, our group recently investigated metal-oxo species in MOFs for the activation of the C-H bond by identifying structure-activity relationships in MOFs based on DFT calculations,[35,36] screening a MOF database to identify promising MOF systems,[37] and investigating triazolate based MOFs with varying metals and anions theoretically.[38,39]

Based on their studies of triazolate based MOFs for C-H bond activation, Rosen *et al.*,[39] proposed the MOF $Zn_5Cl_4(BTDD)_3$, where H_2BTDD = bis(1,2,3-triazolo[4,5-*b*],[4′,5′-*i*])dibenzo[1,4]dioxin, also known as MFU-4l,[40] as a platform material. This MOF is known to be chemically and thermally stable. Furthermore, four of the five Zn ions contained in the metal node can be post-synthetically exchanged with other transition metals[41] and even lithium[42,43] to obtain M_x-MFU-4l (M being the introduced metal and x the number of exchanged ions per unit cell). The exchanged metal sites can in turn provide a basis for a desired catalytic application. Besides the metal itself, also the counter-anion located at the metal node is subject to post-synthetic exchange.[41,44] In this work, we focus on the exchange of Cl^- to OH^-, which has already been experimentally achieved for a range of transition metal substituted M-MFU-4l(OH) materials (M=Cu, Co, Ni).[45–48] See Figure 1 for a representation of the Fe_1-MFU-4l(OH) MOF structure. We limit this investigation to N_2O as the oxygen source[39] for practical reasons and only consider the homolytic methane activation pathway, as it is the most relevant one for iron-oxo active sites.[49] The goal of this work is to achieve insight into the C-H bond activation in methane and the factors that affect the selectivity using a fully periodic model of the MFU-4l platform, including non-local second-sphere effects.

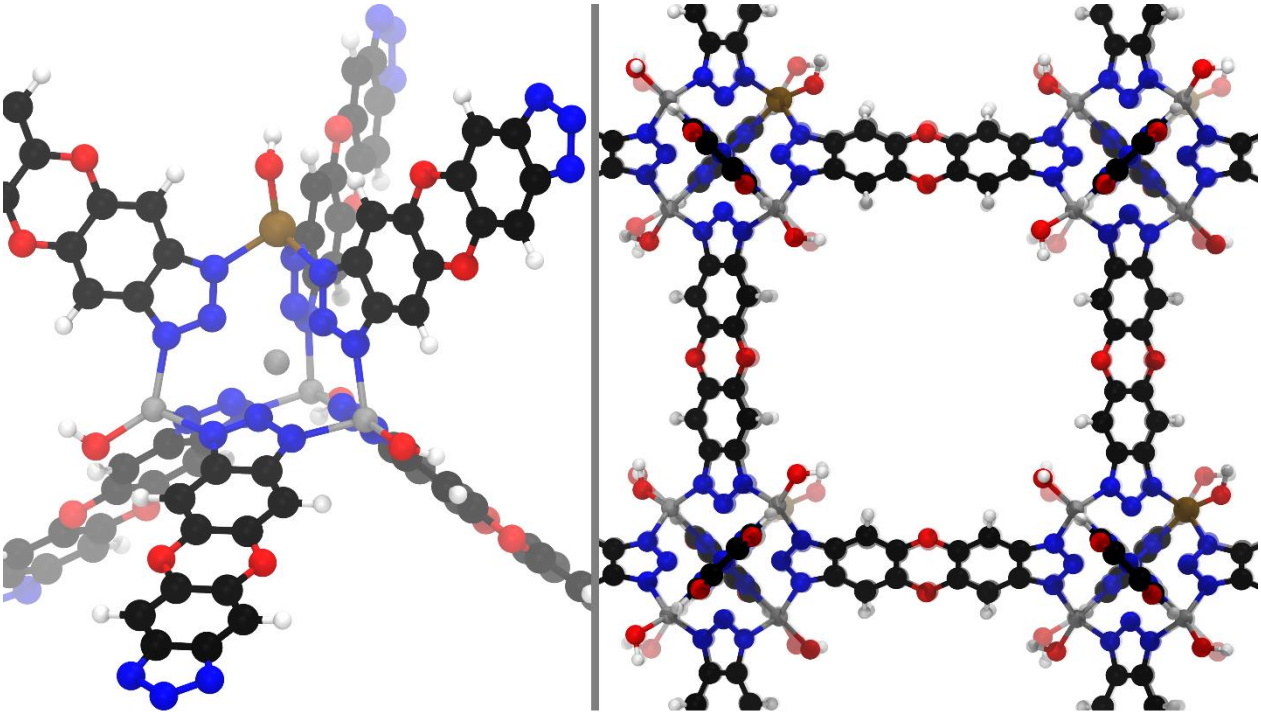

Figure 1: Representation of MOF Fe_1-MFU-4l(OH). Left: node structure containing one iron center. Right: view through the MOF along a square channel. Atoms colored by element: hydrogen white, carbon black, nitrogen blue, oxygen red, iron brown and zinc grey. Reproduced under the terms of the Creative Commons Attribution 4.0 License.[70]

Methods

All periodic calculations were performed using the VASP software in versions 5.4 and 6.2.[50] Tests showed no differences in energies and forces between the two versions; therefore the upgrade to version 6.2 was made during the project to benefit from recent performance improvements. PAW PBE pseudopotentials of version 5.4[51,52] were used. The PBE functional[53] was used in conjunction with the D3BJ dispersion correction method[54,55] at an energy cutoff value of G_{cut} = 800 eV to perform spin unrestricted calculations in the Γ-only approximation. The electronic convergence criterion was set to 10^{-8} eV, and a Gaussian smearing of width 0.01 eV was applied to the orbital occupations. An “accurate” grid (meaning 2*G_{cut} FFT-grid points along every cell vector) was used.

Geometry optimizations and nudged elastic band (NEB) calculations[56–58] employed a force convergence criterion of 0.02 eV/Å. Single point (SP) energy calculations were performed using the range-separated hybrid functional HSE06,[59] also using D3BJ dispersion correction[60] and the same settings as described above.

The cell parameters of the MOF system (170 atoms) were optimized for Fe_1-MFU-4l(OH) (**M**) with one N_2O guest molecule (**M**+N_2O) and kept fixed for all following calculations (see below for details). The singlet, triplet, and quintet spin state energies of **M** and $(Fe{=}O)_1$-MFU-4l(OH) (**MO**) were compared at the PBE optimized geometries using single point HSE06 calculations. The high-spin (HS) quintet state is lowest in energy for both structures and was therefore used throughout this study.

All NEB calculations were performed using five NEB images in the climbing image variant to optimize the transition state using VTST version 184.[61] Initial linear or image dependent pair potential (IDPP)[62] interpolation as included in VTST, and ASE[63] was used to generate initial guesses of the NEB path. A spring constant of 5 eV/Å^2 with nudging was used. Transition state structures from the NEB calculations were further refined using the dimer method.[64–67]

Pre- and postprocessing was conducted using functionality from the ASE[63] and TST packages.[61] Plots were produced using the matplotlib library,[68] and VMD[69] was used for structural representations. The full workflow including all scripts, plots, inputs, and outputs generated in this project are available on Zenodo and NOMAD.[70,71]

Results and Discussion

Base Structure

The Fe_1-MFU-4l(OH) system (labeled **M** in the following, see Figure 1 and Figure 2) consists of two metal nodes per unit cell, one of which includes an iron center. Each metal node contains four tetrahedral positions and one central octahedral Zn^{2+}. Relative energies of the fully optimized structures at the PBE level in spin states S=0, S=1 and S=2 are given in column 2 of Table 1. It can be seen that the high-spin state has by far the lowest energy. We also performed HSE06 single-point calculations on these geometries. These relative energies are reported in column 3, and again the S=2 spin state has the lowest energy. Finally, we took the geometries obtained for the S=2 spin state with PBE and ran HSE06 single-point calculations at S=0, S=1 and S=2. These relative energies are reported in the last column of Table 1. Fixing the geometry at the S=2 optimized structure also does not change the trends, so single point comparisons of the optimized structures can be used for estimating the most likely spin state.

Table 1: Relative energies of the Fe_1-MFU-4l(OH) system depending on spin state (first column) with respect to the energy of spin state S=2. Structures optimized in the respective spin state (column two and three), or fixed at the geometry of the S=2 state (last column). Double slash notation: <Level of theory used for geometry optimization>//<Level of theory used for subsequent single point calculation>. All energy values in kJ/mol.

Spin State	ΔE(PBE//PBE)	ΔE(PBE//HSE06)	ΔE(PBE@S=2//HSE06)
S=1	+52.7	+123.5	+127.5
S=0	+75.1	+176.8	+161.6

After loading the S=2 system with one N_2O molecule per unit cell, a neglectable expansion of the unit cell (ΔV=17.6 Å^3 or 0.2%) is observed after full relaxation of atomic positions and cell parameters. The cell parameters of this loaded cell are used from here on for all calculations.

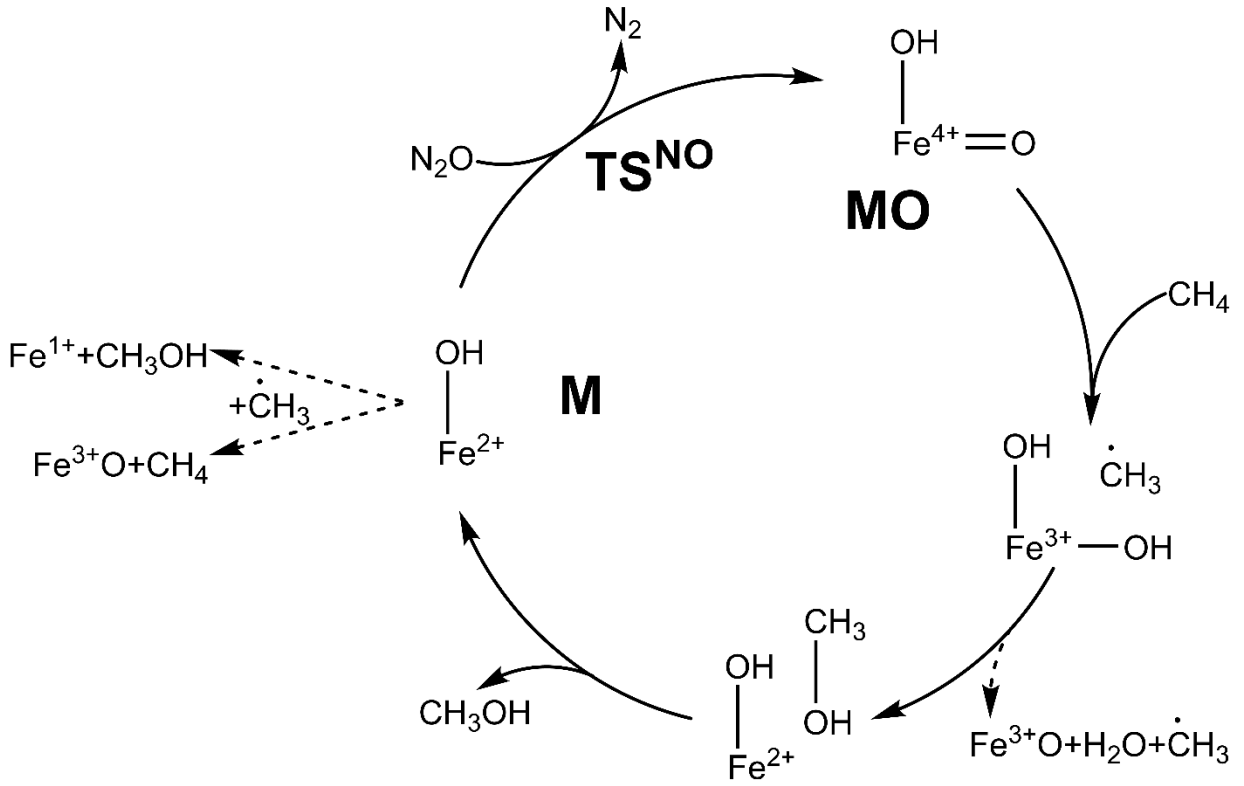

Figure 2: Catalytic cycle of the methane oxidation step (CH_4 to CH_3OH) as studied in this work. MOF backbone omitted for clarity. Dashed arrows represent the studied deactivation pathways of the methane oxidation step. Reproduced under the terms of the Creative Commons Attribution 4.0 License.[70]

The proposed catalytic cycle depicted in Figure 2 begins with the Fe^{2+}(OH) site of the MOF platform (labelled **M)**. Addition of the oxygen source N_2O and breaking of the N-O bond via the transition state **TS^{NO}** yields N_2 and the active iron-oxo species **MO**. Methane can interact with and be activated by the **MO** site, resulting in a methyl radical and $Fe^{3+}(OH)_2$. Recombination of the methyl radical with one OH group in a so-called rebound step leads to adsorbed methanol, which can desorb as the desired product to regenerate the initial MOF site **M**.

Formation of Terminal Iron-Oxo Species

The adsorption energy of N_2O onto the **M** site from the gas phase is -13.2 kJ/mol, of which 102% is contributed by dispersion interactions (PBE level of theory). A single point HSE06 calculation yields an adsorption energy of -15.8 kJ/mol. As expected, the adsorption energy is only slightly influenced by the choice of functional. We therefore only report PBE energies for adsorption and desorption steps to reduce computational costs. The N-O bond splitting exhibits an energy barrier of +119.0 kJ/mol (HSE06; for PBE +70.7 kJ/mol). The corresponding NEB reaction path is shown in Figure 3. This energy barrier is comparable to previously reported DFT data for the creation of iron-oxo species.[72] The energy barrier is also lower (PBE) or close to (HSE06) many calculated energy barriers for N_2O at open metal sites[72–75] that are known to form metal-oxo sites with N_2O in experiments. The results suggest that the activation of **M** to **MO** is feasible in this system.

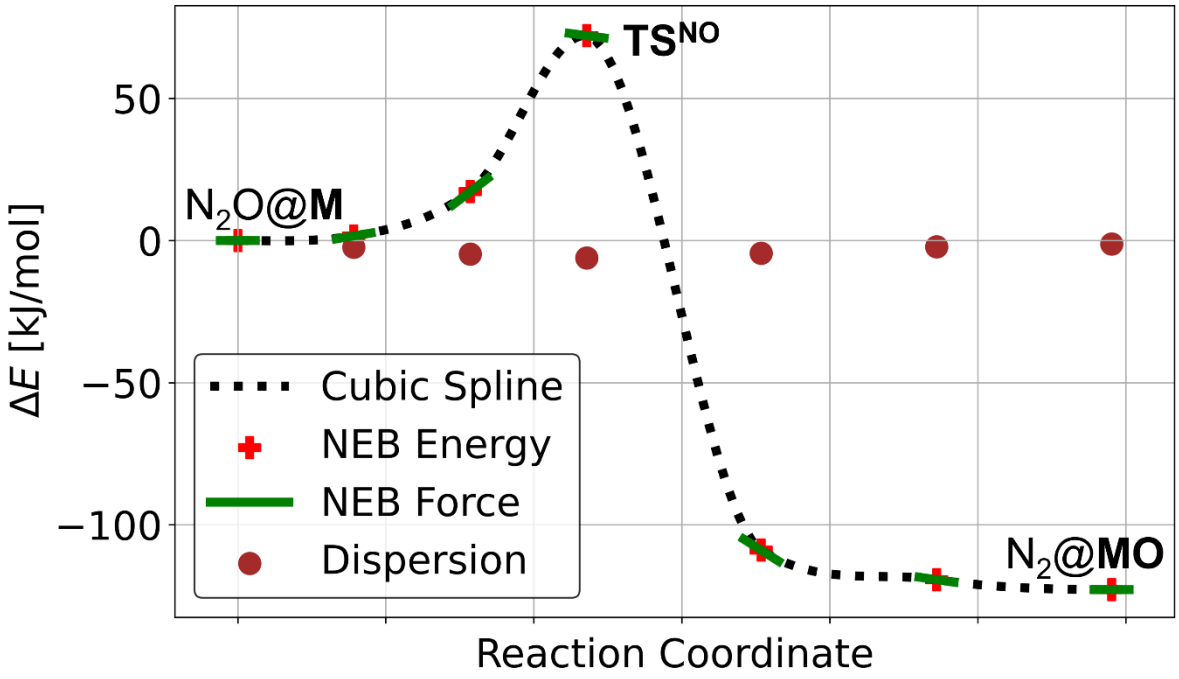

Figure 3: Reaction path of iron oxidation by N_2O as obtained from a climbing image NEB calculation using five images at the PBE level of theory. Relative energies (red crosses) are plotted against the reaction coordinate. A cubic spline interpolation using the energies as well as the gradients (forces along the NEB path) is plotted as a black dashed line. The forces parallel to the NEB path (the derivative of the potential energy surface along the path) are visualized as green bars at each relative energy point. The relative dispersion energies of the NEB images are plotted as dark red circles. Reproduced under the terms of the Creative Commons Attribution 4.0 License.[70]

The S=2 spin state is confirmed for the iron-oxo species **MO** to be lower in energy than S=1 and S=0 (both for PBE and single-point HSE06 calculations). The obtained energies relative to the S=2 state at the SP HSE06 level of theory are ΔE(S=1)=+83.1 kJ/mol and ΔE(S=0)=+114.9 kJ/mol. Therefore, all further calculations employ the S=2 quintet state. For the activation step using N_2O, the S=2 spin state has also recently been found to exhibit the lowest energy barrier for the creation of an iron-oxo species in iron zeolites.[73] Our results are furthermore in line with previous DFT studies of C-H activation on Fe=O species, even though it is known that the S=2 spin state is not necessarily the only reactive state: The spin state may change during the transition from reactants over transition state to products, leading to multi-state reactivity.[76–79] Our HSE06 results are in line with these previous studies and favor the S=2 state for both **M** and **MO**. Also, the error introduced by fixing the spin state of our system for the entire catalytic cycle cannot be expected to be overcome using DFT in any flavor, as DFT in general is not able to resolve subtle energy differences of multi-state reactivity of transition metal systems.[80,81] Fixing the spin state is therefore a necessary choice to achieving our goals. If the S=2 state is indeed the ground state, reactivity of the iron-oxo species in this MOF system can be expected to be high,[10] as experimental evidence for similar systems[82,83] suggests that the S=2 state is more reactive than lower spin states.

Some difference in the N_2O activation energy barrier between the PBE and HSE06 functionals ($\Delta\Delta E_B$, see Figure 4 for a visual comparison) can be expected due to the artificially large electron delocalization of GGA functionals that often occurs in transition metal systems.[84] The magnitude of the difference in this case (48 kJ/mol) is, however, striking. We therefore investigated the origin

of this large deviation by performing calculations for the simple gas-phase reaction $N_2 + \frac{1}{2}O_2 \rightarrow N_2O$ (see SI for details). The reaction energy difference ($\Delta\Delta E_R$) between PBE and HSE06 for this simple gas-phase reaction is, at around 30 kJ/mol, comparable and surprisingly large for such a simple reaction. Our own findings are supported by a larger set of reference calculations in the Computational Chemistry Comparison and Benchmark Database (CCCBD) by NIST.[85] We find good agreement between our calculated $\Delta\Delta E_R$ between HSE06 and PBE in the CCCBD for the reaction $N_2 + \frac{1}{2}O_2 \rightarrow N_2O$. Based on the CCSD(T)=FULL reaction energy from the CCCBD, we argue that the HSE06 calculations should be deemed more trustworthy, as they are much closer to the high-level reference than the PBE results.

Furthermore, the CCCBD data shows a similar behavior for the differences between PBE and HSE06 in the reaction $2O \rightarrow O_2$ as well as for $2N \rightarrow N_2$. On the other hand, for the reaction $CH_4 + \frac{1}{2}O_2 \rightarrow CH_3OH$, this is not the case, and the difference in reaction energy between PBE and HSE06 is only around 6 kJ/mol for large basis set sizes. We therefore conclude that the large differences between PBE and HSE06 observed in this work are not artifacts of our calculations but inherent to DFT. For all cases, HSE06 can be expected to be closer to higher-level calculations and experiments based on the data found in the CCCBD and previous studies by Liu and Kulik.[84]

Methane Oxidation Step

We calculated the adsorption energy of CH_4 at the iron-oxo site **MO** to be -8.7 kJ/mol, of which 87% is contributed by dispersion interactions (PBE level of theory). See Figure 4 for an energy diagram of the PBE and HSE06 relative energies. No energy barrier is observed for the adsorption in an NEB calculation tracking the movement of CH_4 from the center of the pore to the iron-oxo site **MO** (see Figure S2). Based on previous work,[39] we initially hypothesized that a CH_3 radical

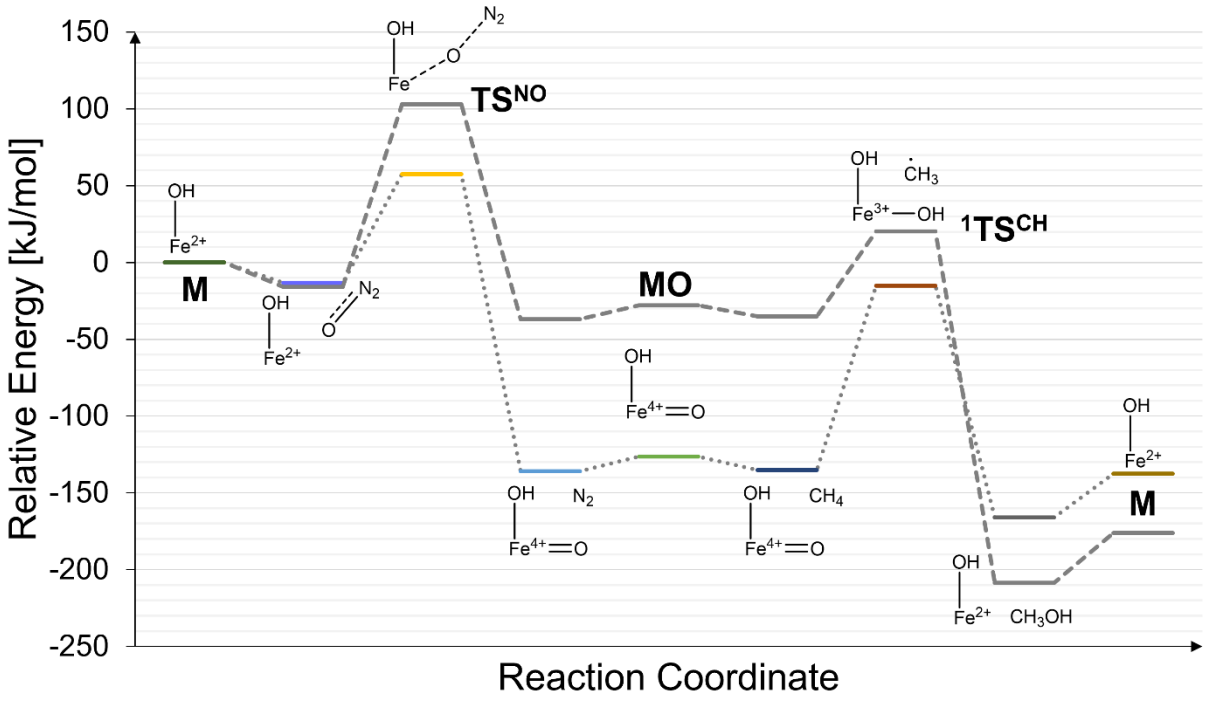

Figure 4: Energy diagram of N_2O activation and first step of methane oxidation. Colored pathway: PBE; grey pathway: HSE06 single points on PBE geometries. Reproduced under the terms of the Creative Commons Attribution 4.0 License.[70]

near the $Fe(OH)_2$ site would be a local minimum on the potential energy surface after the C-H bond activation and therefore chose such a structure as a starting point for a geometry optimization. This optimization of CH_3@$Fe(OH)_2$ resulted in a CH_3 radical structure at the $Fe(OH)_2$ site with forces below the convergence criterion of 0.02 eV/Å, as expected, but a climbing image NEB calculation (Figure S3) showed no transition state between the starting CH_4@**MO** structure and the resulting CH_3@$Fe(OH)_2$ radical structure. Subsequent partial vibrational analysis (Fe and connected OH and CH_3) revealed one low frequency imaginary mode of 27.4*i* cm^{-1} as shown in Figure 5, indicating that this species is a transition state (^{1}**TS**^{CH}) rather than the expected intermediate. The CH_3 species in ^{1}**TS**^{CH} is weakly physisorbed with a binding energy of -10.1 kJ/mol (HSE06; for PBE -11.3 kJ/mol) at the $Fe(OH)_2$ site. Of this binding energy, 71% (65% for PBE) of the adsorption energy is contributed by dispersion interactions.

In the proposed mechanism, the CH_3 radical reacts with an OH group to from a bound methanol molecule. We find an overall reaction energy ΔE(CH_4@**MO** → CH_3OH@**M**) of -173.5 kJ/mol (HSE06; for PBE -30.9kJ/mol). Including ad- and desorption energies, the overall reaction energy for CH_4 + **MO** → CH_3OH + **M** is -148.4 kJ/mol (HSE06; for PBE -11.1 kJ/mol). For comparison, we calculated reaction energies for syngas creation, complete oxidation, and the C-H bond strength using the same methodology. The reaction energies are given in Table 2. Contrary to the strong functional dependence of reaction energies discussed for the N_2O bond breaking above, the functional dependence is much smaller for the simple reactions in Table 2, with the largest deviation between HSE06 and PBE being only 12 kJ/mol. For the MOF system, however, the difference between HSE06 and PBE is again very large, with a value of $\Delta\Delta E_R$(PBE-HSE06) = +142.6 kJ/mol. We can therefore conclude that the difficulties of DFT in this case lie in the description of the active metal species involved and not within the small guest molecules in contrast to the reaction of N_2O with **M**.

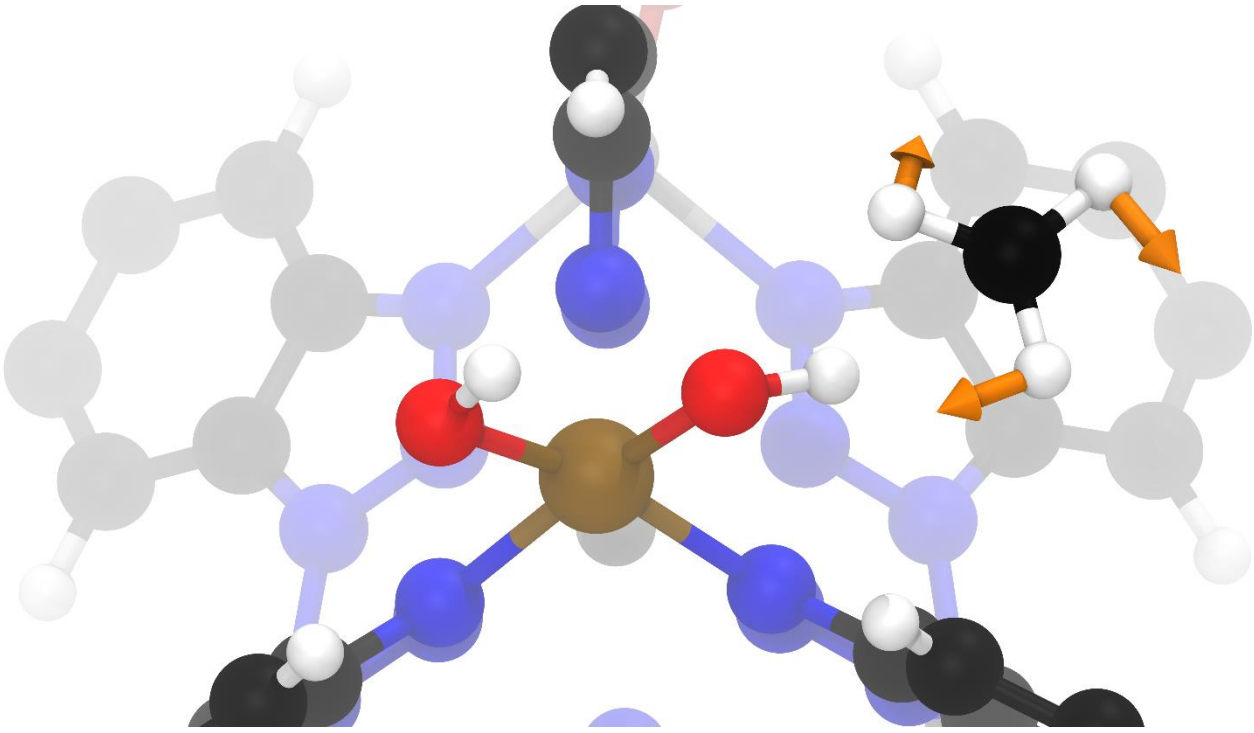

*Figure 5: Visualization of the imaginary vibrational mode at 27.4i cm^{-1} observed in the ^{1}**TS**^{CH} state. Arrows represent the atomic displacements corresponding to this mode. Reproduced under the terms of the Creative Commons Attribution 4.0 License.*[70]

Table 2: Reaction energies of syngas creation, complete oxidation, and C-H bond strength of methane at the HSE06 and PBE levels of theory from periodic calculations using the same methodology and cell as the MOF calculations.

Reaction	HSE06 [kJ/mol]	PBE [kJ/mol]
$CH_4 + 0.5O_2 \rightarrow CO + 2H_2$	+72.4	+64.5
$CH_4 + 2O_2 \rightarrow CO_2 + 2H_2O$	-748	-736
$CH_4 \rightarrow CH_3 + H$	+458	+460
CH_4 + **MO** → CH_3OH + **M**	-148	-11.1

If we take the methyl radical as the relevant transition state (^{1}**TS**^{CH}), the energy barrier (ΔE_B) for H abstraction at the **MO** site is +55 kJ/mol (HSE06; approx. +125 kJ/mol for PBE), which is comparable to values of other well performing iron-oxo sites from our group.[39,72] However, as noted above, we expected the methyl radical to be a stable intermediate, not a transition state. To complete the analysis of the C-H bond activation step, we performed two NEB calculations: one from CH_4@**MO** to ^{1}**TS**^{CH} and another from ^{1}**TS**^{CH} to CH_3OH@**M**. Surprisingly, these two NEB calculations, when combined from CH_4@**MO** to CH_3OH@**M** (Figure 6, combined from Figures S3 and S4), show that there is a prominent energy plateau region around ^{1}**TS**^{CH}. Further calculations showed that there are two transition states within 6 kJ/mol of each other with little geometric differences within the plateau region. As discussed earlier, the limitations of DFT in this system, will make a detailed exploration of subtle energy differences on this plateau of the potential energy surface difficult,[80,81] but for our purposes here the exact shape of the plateau region is not needed. The presence of such a plateau region is unusual and, to the best of our knowledge, new for iron-

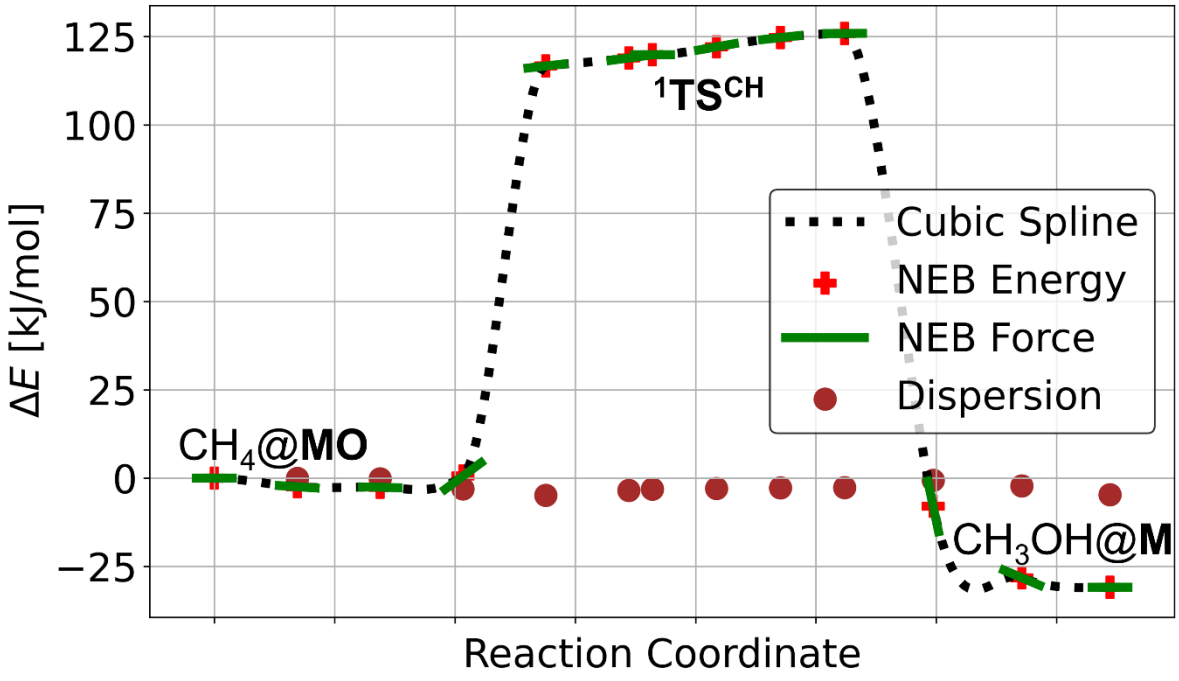

*Figure 6: Reaction pathway of CH_4@**MO** via ^{1}**TS**^{CH} to CH_3OH@**M** at the PBE level of theory. The graph includes two NEB calculations, first from CH_4@**MO** to ^{1}**TS**^{CH} and second from ^{1}**TS**^{CH} to CH_3OH@**M** with five NEB images each. The plateau region of the weakly physisorbed CH_3 radical is clearly visible. Reproduced under the terms of the Creative Commons Attribution 4.0 License.*[70]

oxo systems. It could have major implications for the design of reactive pockets for the methane oxidation process, as it extends the usual CH_3 radical rebound reaction mechanism.

The energy needed to cleave the C-H bond at the **MO** site (55 kJ/mol at the HSE06 level of theory) is almost one order of magnitude lower than the energy barrier in the gas phase (Table 2), nicely showcasing the need for a catalyst. Also, the standard industrial route via syngas already exhibits a distinct thermodynamic penalty compared to the direct catalytic route, even without considering additional practical issues associated with high temperature and pressure.

Similar to the N_2O activation step, a significant difference in the value of the energy barrier is again observed between PBE and HSE06, with values of 55 kJ/mol from HSE06 and 125 kJ/mol from PBE. However, the sign of the difference is inverted, meaning that the barrier is higher in PBE than in HSE06 for the C-H bond breaking (see also Figure 4). Since the difference between the two functionals is inverted for the C-H bond breaking step compared to the N-O bond breaking step, the overall reaction energy of the entire catalytic cycle does not differ as strongly between PBE and HSE06 as the two individual reaction steps. However, the step with the highest energy barrier is the formation of the iron-oxo species according to the HSE06 energy profile, whereas the step with the highest energy barrier is the C-H activation according to the PBE profile. The higher energy barrier for the N-O step compared to the C-H bond breaking is in line with previous PBE, PBE+U and M06-L based studies by Snurr and co-workers.[37,39,72,86]

The radical nature of the methyl $^{1}\mathbf{TS}^{\mathbf{CH}}$ structure can be clearly seen in the visualization of the magnetization density on the right side of Figure 7. One unpaired electron is located on the methyl, and the remaining three unpaired electrons of the same spin are located around the iron center. As Feldt *et al.*[76] suggest that the CH_3 radical structure can also be in an antiferromagnetically coupled (AFM) state with an S=2.5 iron center and an S=0.5 CH_3 radical, we investigated this possibility. Our HSE06 SP calculations on the $^{1}\mathbf{TS}^{\mathbf{CH}}$ structure, however, favor the high spin S=2 state over the AFM S=2 state by 20.3 kJ/mol. The weak methyl-iron interaction (the methyl radical is only physisorbed, see above) could be useful for maintaining an active catalyst, as a strong methyl-iron bond can be expected to increase the creation of unwanted carbene and water,[87] which poison the catalyst.

The lack of a stable (no imaginary frequencies, i.e. a local minimum on the potential energy surface) methyl radical state in the energy plateau region (see Figure 4 and Figure 6) could be due to the high spin density located at the oxo oxygen of the **MO** species (see left side of Figure 7). Previously, the creation of an iron-oxyl species has been discussed as promoting activity towards C-H activation and being dependent on a large amount of unpaired electron density at the oxygen atom.[88–90] The high spin density at the oxo oxygen in our system could, therefore, be responsible for the relatively low energy barrier for H abstraction. Furthermore, we do not observe a stable (local minimum) intermediate involving a methyl radical (see right side of Figure 7). The electronic structure of the $Fe(OH)_2$ system here seems to be the reason for this, as we do not observe any charge transfer from or onto the methyl radical, nor any structural changes compared to a free methyl radical. We therefore propose that the high spin density together with the low stability of the $Fe(OH)_2$ system are the main reasons for the observed energy plateau between CH_4@**MO** and CH3OH@**M**. From this observation, we suggest a single-step reaction mechanism, in contrast to a two-step mechanism involving a stable methyl radical. This could enhance kinetics significantly and thereby lower the chance of CH_3 radical desorption.[25]

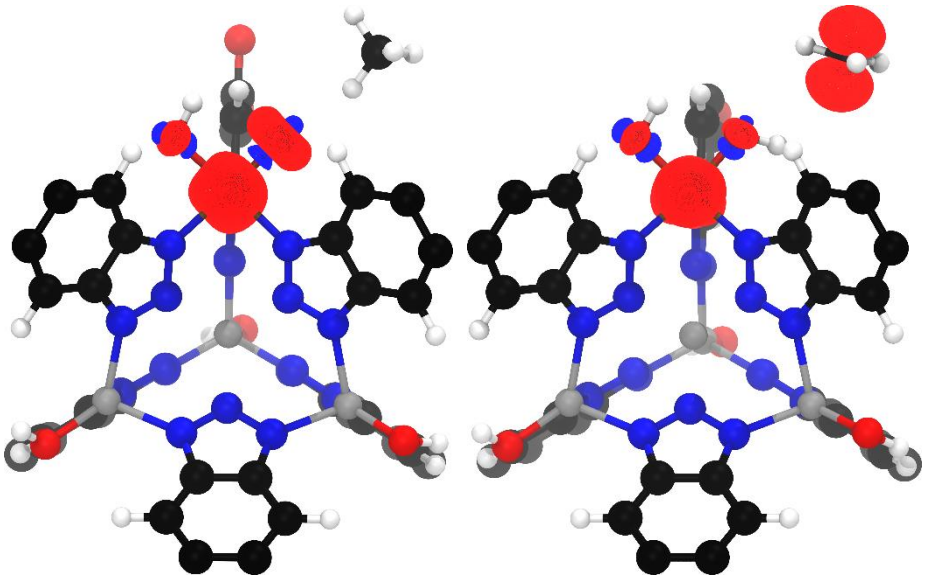

*Figure 7: Magnetization density of the CH_4@**MO** (left) and ^{1}**TS**^{CH} structures (right) plotted at an isovalue of ±0.05 e/Å^3. Reproduced under the terms of the Creative Commons Attribution 4.0 License.*[70]

The methanol desorption energy is +28.5 kJ/mol (PBE). In our initial calculations, the bound methanol was oriented with its OH group pointing away from the Fe-OH group after its formation. A more stable orientation with a hydrogen bond between Fe-OH and HO-CH_3 results in a slightly higher desorption energy (+35.2 kJ/mol PBE). Both values are, however, much lower than previous MOF and cluster results, that are in the range of +77 to +150 kJ/mol.[72] A low desorption energy is beneficial for removing the product from the framework and thereby hindering its overoxidation. However, the same argument could be reversed: low desorption energies could lead to larger amounts of secondary oxidation products, as the methanol can easily transfer to another active site.[91] Which argument is more relevant will therefore depend on the chosen operation mode of the catalyst system, either continuous operation (lower desorption energy of methanol is better) or "stepped conversion" operation (higher adsorption energy is better).

Deactivation Pathways

To better understand the reactivity and selectivity, it is important to consider possible deactivation pathways. We therefore studied three possible deactivation pathways for the active site. First, following the work by Snyder et al.,[25] we considered the possibility of CH_3 radical desorption and subsequent reaction with other **M** sites. As discussed above, the adsorption energy of the CH_3 radical is only around -10 kJ/mol, of which 65% is from dispersion interactions. Desorption of the radical is therefore energetically possible. A desorbed radical might react in two ways with an adjacent **M** site, creating either methanol and an Fe^+ site or methane and an $[Fe{=}O]^{+1}$ site:

$$Fe^{+2}(OH)^{-1} + CH_3 \longrightarrow Fe^{+1} + CH_3OH\ (ads)$$

$$Fe^{+2}(OH)^{-1} + CH_3 \longrightarrow [FeO]^{+1} + CH_4\ (ads)$$

The reaction energies ΔE(HSE06) are +5 kJ/mol for the creation of CH_3OH (ads) and -51 kJ/mol for the formation of CH_4 (ads). However, when performing NEB calculations for the pathway from methyl to methanol, an intermediate minimum $[Fe{=}O]^{+1}$ structure is encountered. Therefore, the creation of an Fe^+ site is not likely to occur. If and how the deactivated $[Fe{=}O]^{+1}$ site could be

reactivated is not further investigated here. The desorption energy of CH_4 to the gas phase after this reaction is +30.0 kJ/mol (PBE), for CH_3OH it is +74.5 kJ/mol (PBE).

In the second deactivation pathway, the MOF site corresponding to the **$^1TS^{CH}$** species could – instead of reacting to form methanol – undergo H_2O elimination by reaction of the two OH groups and creation of an Fe^{3+}=O site:

$$Fe^{+3}(OH)_2 \longrightarrow Fe^{+3}O + H_2O\ (ads)$$

This reaction exhibits an energy barrier of +97.0 kJ/mol (HSE06; for PBE +75.7 kJ/mol) and a total reaction energy of ΔE = +90.7 kJ/mol (HSE06; for PBE +62.0 kJ/mol). Considering that this energy barrier must be added to the energy barrier to reach **$^1TS^{CH}$**, we suggest that this reaction is unlikely to occur. In the third deactivation pathway, the reaction of methanol with an **M** site could lead to an iron-bound methoxy species $FeOCH_3$ and water (ads). We find, that the reaction energy for this reaction is +4.7 kJ/mol (HSE06; for PBE -0.02 kJ/mol), making it an energetically slightly unfavorable but possible side reaction, considering the desorption energy of water into the gas phase is 34.1 kJ/mol. However, the so formed iron-methoxy species can be expected to be subject to hydrolysis due to the slightly higher relative energy of the iron-methoxy species with respect to the **M** site.

The reactions of desorbed methyl radicals with **M** sites can therefore be considered to play the most important role in catalyst poisoning. However, due to the plateau nature of the potential energy surface in the methane activation step, desorption of the methyl radical during the reaction is very unfavorable.The third deactivation pathway is very similar to the problem of preventing overoxidation of methanol discussed next.

Methanol Oxidation Step

Understanding potential over-oxidation reactions – i.e. further oxidation of the product methanol – is also an important consideration for the overall reaction selectivity. For this reason, we further studied the activation of methanol on the active site **MO**. The catalytic cycle is depicted in Figure 8, starting with formation of the active species **MO** from the reaction of **M** and N_2O as above. The adsorption energy of CH_3OH onto the **MO** site is -31.3 kJ/mol (HSE06; for PBE -36.5 kJ/mol). As expected, this is more exothermic (approximately 23 kJ/mol) than CH_4 adsorption at the same site, as methanol exhibits a dipole moment. Once adsorbed, two relevant pathways were investigated: C-H activation or O-H activation.

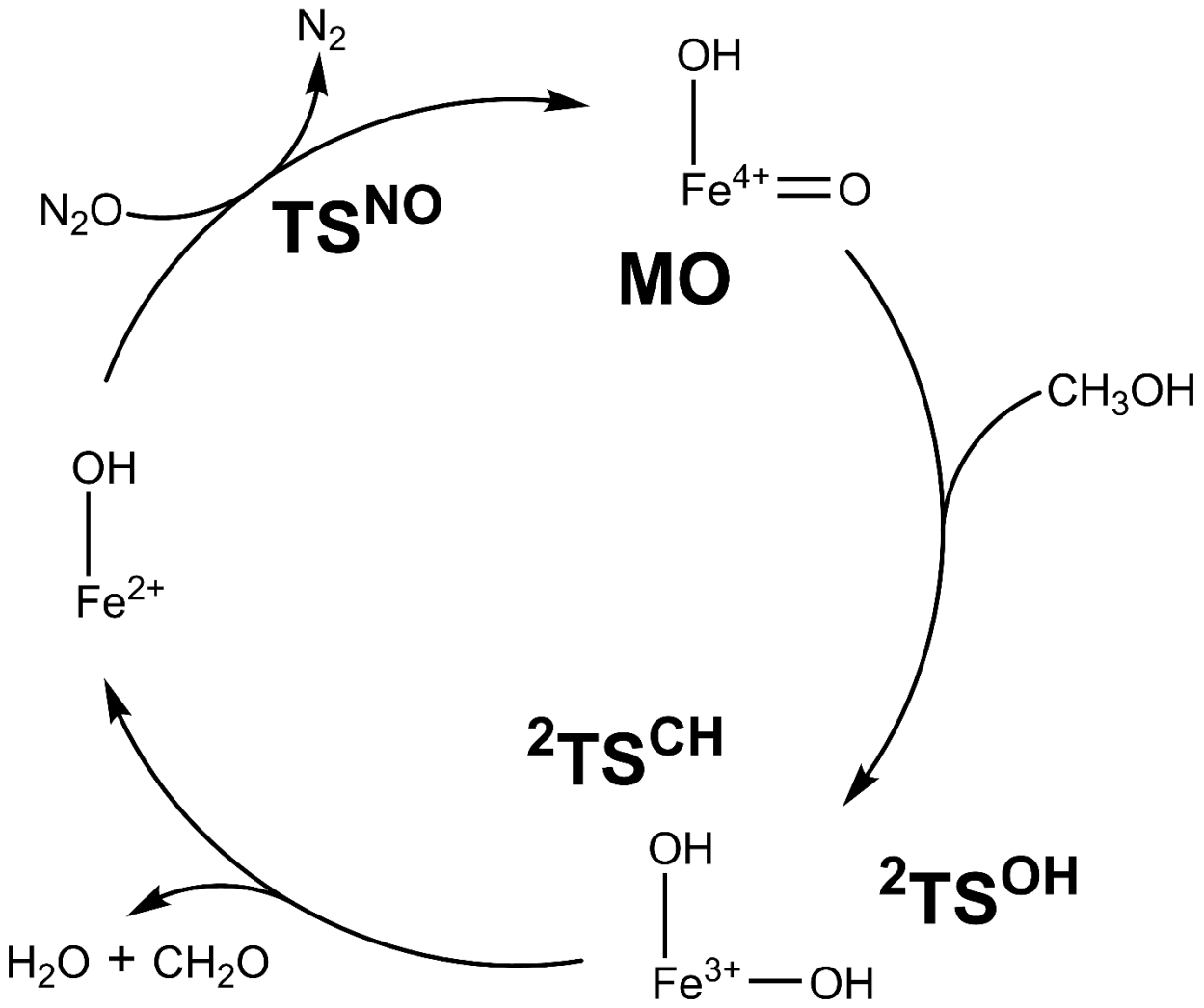

Figure 8: Catalytic cycle of the methanol oxidation step as studied in this work. MOF backbone omitted for clarity. Reproduced under the terms of the Creative Commons Attribution 4.0 License.[70]

For the activation of the C-H bond of methanol, we find an activation energy of +20.1 kJ/mol (HSE06; for PBE +82.7 kJ/mol) via the transition structure **^{2}TS^{CH}** (see also Table 3). The reaction energy to the product radical ΔE(CH_3OH@**MO**→CH_2OH@$Fe(OH)_2$) is +9.9 kJ/mol (HSE06; for PBE +71.5 kJ/mol). The energy diagram is plotted in Figure 9. As in the methane oxidation step, the differences in reaction energies between PBE and HSE06 are large. Overall, a smaller activation energy is observed for the C-H activation of methanol than for the C-H activation of methane, as expected.

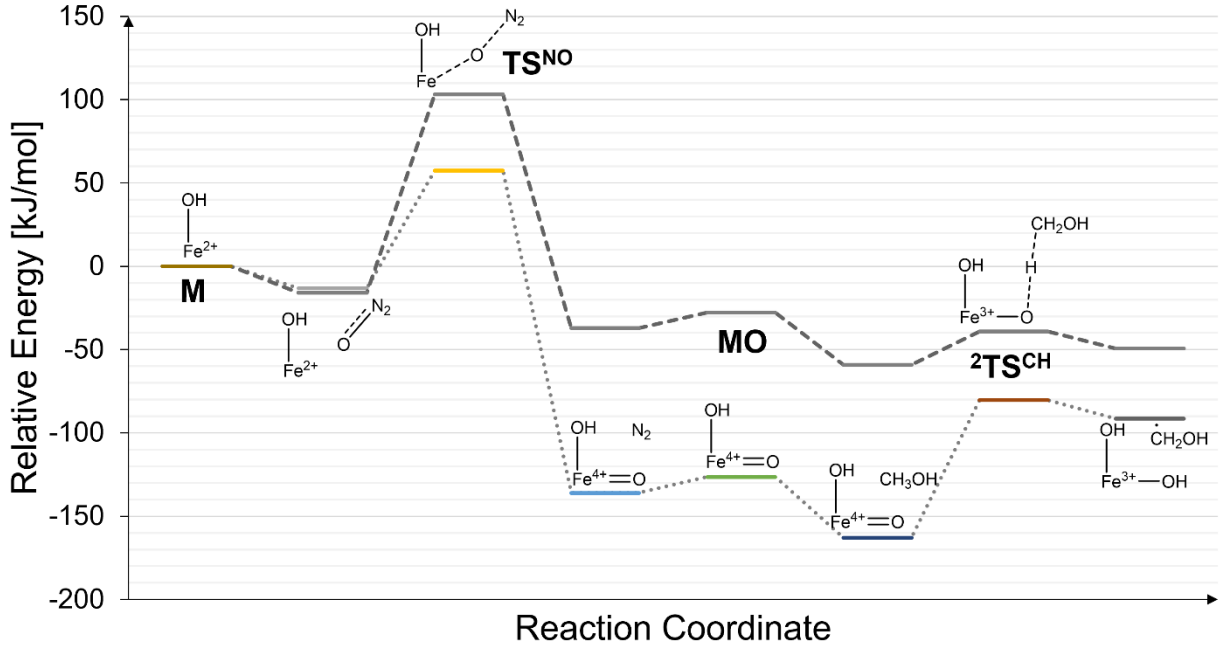

Figure 9:: Energy diagram of the second oxidation step activating a C-H bond of methanol. Colored pathway: PBE, grey pathway: HSE06 single points on PBE geometries. Arbitrary reaction coordinate with equidistant steps between structures. Reproduced under the terms of the Creative Commons Attribution 4.0 License.[70]

For the case of the O-H bond activation, we were unable to locate a local minimum using a CH_3O radical as the product. Geometry optimization of this hypothesized CH_3O radical together with $Fe(OH)_2$ results in formation of CH_2O, H_2O and Fe(OH), which agrees well with our chemical intuition about the stability of a CH_3O radical. The reorganization of the atoms during geometry optimization into CH_2O and H_2O is therefore not surprising. The energy barrier for **^{2}TS^{OH}** is +62.7 kJ/mol (HSE06; for PBE +118.0 kJ/mol) and the reaction energy ΔE(CH_3OH@**MO**→[CH_2O+H_2O]@**M**) is -161.1 kJ/mol (HSE06; -25.9 kJ/mol for PBE). As can be seen from Table 3, the energy barrier is higher for **^{2}TS^{OH}** than for **^{2}TS^{CH}**.For PBE it is also still slightly lower than for the first C-H energy barrier in methane (**^{1}TS^{CH}**), but the HSE06 energy barrier is higher for **^{2}TS^{OH}** than for **^{1}TS^{CH}**. The C-H bond activation can therefore be expected to be the most relevant pathway for methanol oxidation and unwanted overoxidation.

Table 3: Energy barriers of first and second hydrogen abstraction steps. All energy values in kJ/mol.

	HSE06	PBE
^{1}TS^{CH}	~55	~125
^{2}TS^{CH}	+20.1	+82.7
^{2}TS^{OH}	+62.7	+118.0

Overall, the obtained results for the methanol oxidation step highlight once again the need to prevent methanol overoxidation.[6] The inherently weaker C-H bonds of methanol compared to the C-H bonds of methane make this a necessary design feature of any potential catalyst.

Diffusion

For the design of a methanol-protecting environment, the interactions of guest molecules with the other parts of the framework beyond the active site are crucial. We therefore analyzed the host-guest interactions of the Fe_1-MFU-4l(OH) system with the reactants and products. Looking into the NEB paths of reactants and products (N_2, CH_4 and CH_3OH) from the center of the pore to the **M** or **MO** site, we observe no barriers (Figures S1, S2 and S5). However, the MFU-4l framework exhibits one peculiarity: Neighboring pores, although lined by the same linkers, exhibit different pore volumes as the anions coordinating to the metal node only point into every second pore, making it smaller than all the surrounding pores (see Figure 10). Previously, attempts were made to use this characteristic feature e.g., for H_2/D_2 sieving in the small pore variant MFU-4.[92] To

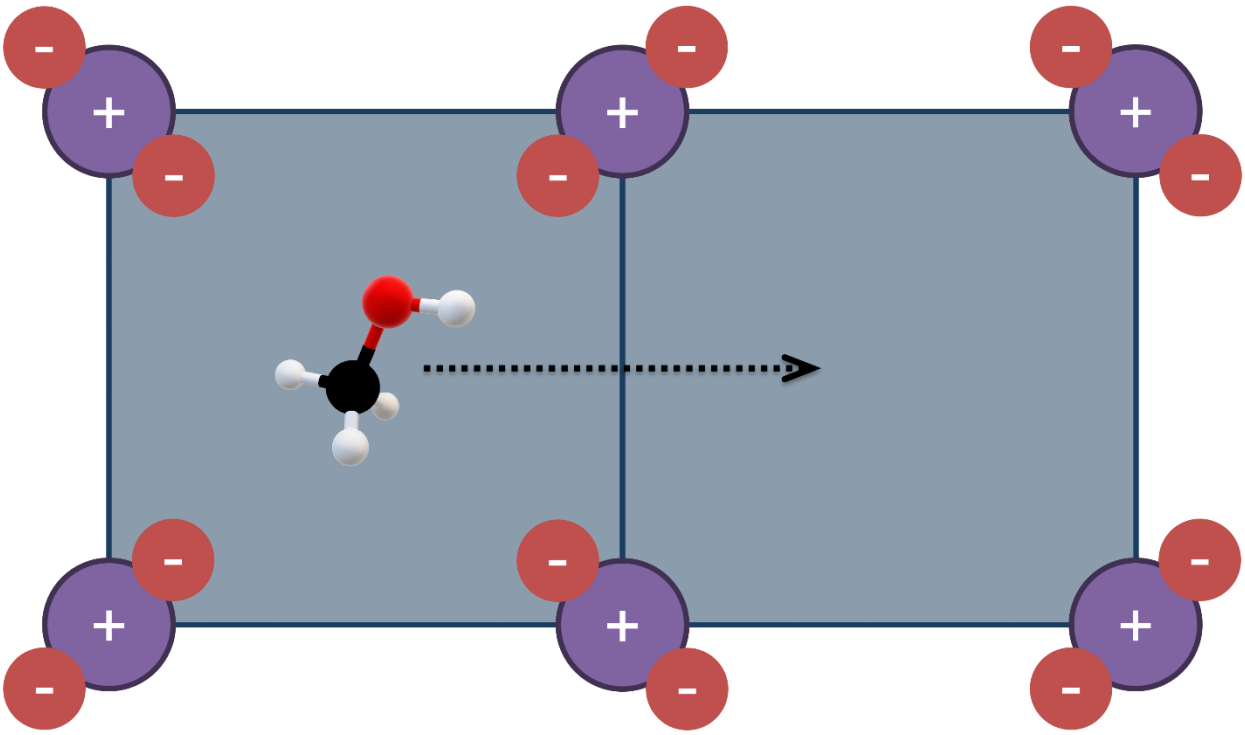

Figure 10: Cartoon of two neighboring pores in MFU-4l and the orientation of the OH anions. Blue lines represent BTDD linkers, purple circles zirconium nodes and red circles OH anions. The path of a methanol molecule from the smaller to the larger pore is sketched by a dotted black arrow.

investigate possible barriers for guest molecules to move through the Fe_1-MFU-4l(OH) system, we therefore placed all guest molecules (CH_3, CH_3OH, CH_4, H_2O, N_2 and N_2O) in the center of the small and large cavities and performed NEB calculations between the two differently sized pores (see Figure 10). All diffusion calculations used PBE, as adsorption energies do not show a strong functional dependence throughout this work. Resulting NEB paths are given in Figures S11-16. The pore-to-pore minimum energy paths exhibit a slight minimum in the middle, i.e., close to the linkers. Optimizing the guest molecules at the window position of the previous NEB, i.e., close to linkers, converges instantaneously. The observed forces are very weak (below the convergence criterion of 0.02 eV/ Å) and energy differences are very small: all guest molecules exhibit energy

differences between the window and center of the pore of less than 1.5 kJ/mol except for H_2O where the energy difference is 2.5 kJ/mol. All molecules slightly favor the window position over the center of the pore. The energy difference between the centers of the large and small pores is also very small (the largest energy difference being 1.1 kJ/mol for CH_3OH with a preference for the smaller cavity). The small energy differences between the center of the pore and the pore windows are within the accuracy of the methodology. Also, no significant forces are observed at either the pore window or center of the pore, suggesting a rather flat potential energy surface throughout the pore system. This fits well with the small size of the adsorbates compared to the large pore and window sizes. Using PoreBlazer 4.0[93] with default settings, we calculated the pore limiting diameter to be 9.4 Å (manually measured distances between hydroxy oxygens are approx. 9 Å). The diameters of the two pores, as determined by PoreBlazer, are 12.0 Å and 16.5 Å.

Table 4: Guest molecule adsorption energies (ΔE(ads)) and their respective dispersion contributions (Disp.) on Zn and Fe sites as calculated at the PBE level of theory. Specification of the iron site given after the energy value inside the table. All energy values in kJ/mol.

	ZnOH Site		**Fe Site**	
Guest	ΔE(ads)	Disp.	ΔE(ads)	Disp.
CH_3	-15.2	90%	-11.3 **$^1TS^{CH}$**	65%
CH_3OH	-52.7	36%	-35.2 **M** / *-34.5* ***MO***	47% / 35%
CH_4	-13.0	107%	-8.7 ***MO***	87%
H_2O	-47.5	21%	**-**37.2 **M** / -47.8 **MO**	23% / 18%
N_2	-10.7	106%	-9.6 ***MO***	67%
N_2O	-18.2	83%	-13.2 ***M***	102%

As the pore windows are too large to significantly influence diffusion, we further investigated the adsorption energies of the guest molecules on a Zn-only node, to evaluate the potential role of non-catalytic nodes in the guest's mobility within the MOF. We calculated these adsorption energies by manually placing the guest molecules close to a Zn metal atom and performing a geometry optimization. Resulting adsorption energies are given in Table 4, together with adsorption energies on the active iron site. As observed for the methanol adsorption on the **M** site, the hydrogen-bonded conformation exhibits a significantly stronger interaction with the metal node than the conformation without a hydrogen bond, and the adsorption energy of methanol with a hydrogen bond is therefore comparable to that of water. The adsorption energy of methanol on the Zn site is furthermore significantly stronger (−52.7 kJ/mol) than on the **M** and **MO** sites (−35.2 and −34.4 kJ/mol), which could be useful to prevent overoxidation by binding product methanol molecules to a Zn site until removal from the pores. The strongest adsorption energy of methanol found on the linker is only -22.8 kJ/mol. An NEB calculation of the methanol movement from one Zn site across a linker to another Zn site results in an energy barrier of +39.6 kJ/mol (PBE, see Figure S17). From this we conclude that the linker-methanol interactions are not strong enough along the entire linker to facilitate transport of methanol at the pore walls. The difference between the energy barrier along the linker and desorption to the center of the pore is less than 13.1 kJ/mol for methanol. Therefore, diffusion of methanol should be determined mainly by the interaction strength with the Zn sites, not by the pore size or linkers. All other guests show no significant preference for binding to Zn versus Fe sites (see Table 4), and their diffusion is therefore expected to be influenced mainly by the relatively small host-guest interactions (which are dispersion dominated). These insights suggest one major route to achieve a higher selectivity towards methanol in a non-continuous setup of this catalytic system: exploiting the stronger zinc-methanol interactions to immobilize methanol at abundant non-reactive sites.

Conclusions

We studied the oxidation of methane using N_2O in Fe_1-MFU-4l(OH) using periodic DFT calculations. We predict that iron sites introduced into MFU-4l by post-synthesis metal exchange should be active for the cleavage of the C-H bond in methane. The iron sites are predicted to be susceptible to activation by N_2O to provide highly active iron-oxo species. The rate-determining step for the oxidation of methane is predicted to be the creation of the iron-oxo species, not the C-H bond breaking. Our DFT calculations suggest a single-step process for C-H activation with no stable, local minimum CH_3 radical intermediate which differs from the traditional radical rebound mechanism. This could be beneficial for the kinetics of the reaction and reduce possible deactivation pathways of the catalyst. Therefore, we suggest the Fe-MFU-4l(OH) system for further experimental investigation as an oxidation catalyst for the methane to methanol conversion. In the future, we also suggest that by rationally modifying the surrounding of the Fe ions by substituting the H atoms on the BTDD linker, the activation energy of the second oxidation step could be influenced. A possible substitution could e.g. be used to create a hydrophobic pocket that inhibits methanol from approaching the active site.

Furthermore, we observe that relative energies of the studied systems are highly dependent on the functional used. GGA functionals are known to provide incorrect mechanistic insights if blindly applied to transition metal catalysts, and we show that this is even true for very simple main-group reactions like the cleavage of the N-O bond in N_2O. Hybrid functionals overcome these problems to a large extent. We therefore advise the community to take special care when choosing functionals, even for very small and simple molecules as N_2O. A minimum requirement should be the application of +U corrections[94,95] (with careful choice of the U values used) or more recent developments in the field of approximate DFT methods like MO-DFT+U.[96] The accuracy and transferability of the used functionals and methods should always be investigated for each reaction and compared to database values for similar small systems to prevent misguided conclusions. Recent developments in GPU acceleration make the use of hybrid functionals possible and should be applied whenever feasible.

Author Contributions

Patrick Melix: Conceptualization, Methodology, Software, Validation, Formal analysis, Investigation, Data Curation, Writing - Original Draft, Writing - Review & Editing, Visualization. Funding acquisition

Randall Q. Snurr: Resources, Writing - Review & Editing, Supervision, Project administration, Funding acquisition

Conflict of Interest

R.Q.S. has a financial interest in the start-up company NuMat Technologies, which is seeking to commercialize metal−organic frameworks. P.M. declares no competing financial interests, and all authors declare no competing non-financial interests.

Acknowledgements

We thank Andrew Rosen for fruitful discussions and support during this project. P.M. thanks Ralf Tonner-Zech for his support and a nice place to work. This research was supported in part through the computational resources and staff contributions provided for the Quest high performance computing facility at Northwestern University which is jointly supported by the Office of the Provost, the Office for Research, and Northwestern University Information Technology. This research used resources of the National Energy Research Scientific Computing Center (NERSC), a U.S.

Department of Energy Office of Science User Facility located at Lawrence Berkeley National Laboratory, operated under Contract No. DE-AC02-05CH11231 using NERSC award BES-ERCAP0020094. R.Q.S. acknowledges funding by the Institute for Catalysis in Energy Processes (ICEP) via the U.S. Department of Energy, Office of Science, Office of Basic Energy Sciences (award number DE-FG02-03ER15457). P.M. acknowledges funding by the Alexander von Humboldt foundation through a Feodor Lynen fellowship.

References

(1) Faramawy, S.; Zaki, T.; Sakr, A.A.-E. Natural gas origin, composition, and processing: A review. *J. Nat. Gas Sci. Eng.* **2016**, *34*, 34–54. DOI: 10.1016/j.jngse.2016.06.030.
(2) Shindell, D. T.; Faluvegi, G.; Koch, D. M.; Schmidt, G. A.; Unger, N.; Bauer, S. E. Improved attribution of climate forcing to emissions. *Science* **2009**, *326* (5953), 716–718. DOI: 10.1126/science.1174760.
(3) Schiaroli, N.; Volanti, M.; Crimaldi, A.; Passarini, F.; Vaccari, A.; Fornasari, G.; Copelli, S.; Florit, F.; Lucarelli, C. Biogas to Syngas through the Combined Steam/Dry Reforming Process: An Environmental Impact Assessment. *Energy Fuels* **2021**, *35* (5), 4224–4236. DOI: 10.1021/acs.energyfuels.0c04066.
(4) Olivos-Suarez, A. I.; Szécsényi, À.; Hensen, E. J. M.; Ruiz-Martinez, J.; Pidko, E. A.; Gascon, J. Strategies for the Direct Catalytic Valorization of Methane Using Heterogeneous Catalysis: Challenges and Opportunities. *ACS Catal.* **2016**, *6* (5), 2965–2981. DOI: 10.1021/acscatal.6b00428.
(5) Sushkevich, V. L.; Palagin, D.; Ranocchiari, M.; van Bokhoven, J. A. Selective anaerobic oxidation of methane enables direct synthesis of methanol. *Science* **2017**, *356* (6337), 523–527. DOI: 10.1126/science.aam9035.
(6) Ravi, M.; Ranocchiari, M.; van Bokhoven, J. A. The Direct Catalytic Oxidation of Methane to Methanol-A Critical Assessment. *Angew. Chem. Int. Ed.* **2017**, *56* (52), 16464–16483. DOI: 10.1002/anie.201702550.
(7) Dinh, K. T.; Sullivan, M. M.; Serna, P.; Meyer, R. J.; Dincă, M.; Román-Leshkov, Y. Viewpoint on the Partial Oxidation of Methane to Methanol Using Cu- and Fe-Exchanged Zeolites. *ACS Catal.* **2018**, *8* (9), 8306–8313. DOI: 10.1021/acscatal.8b01180.
(8) Schulz, C. E.; Castillo, R. G.; Pantazis, D. A.; DeBeer, S.; Neese, F. Structure-Spectroscopy Correlations for Intermediate Q of Soluble Methane Monooxygenase: Insights from QM/MM Calculations. *J. Am. Chem. Soc.* **2021**, *143* (17), 6560–6577. DOI: 10.1021/jacs.1c01180.
(9) Ciano, L.; Davies, G. J.; Tolman, W. B.; Walton, P. H. Bracing copper for the catalytic oxidation of C–H bonds. *Nat. Catal.* **2018**, *1* (8), 571–577. DOI: 10.1038/s41929-018-0110-9.
(10) Engelmann, X.; Monte-Pérez, I.; Ray, K. Oxidation Reactions with Bioinspired Mononuclear Non-Heme Metal-Oxo Complexes. *Angew. Chem. Int. Ed.* **2016**, *55* (27), 7632–7649. DOI: 10.1002/anie.201600507.
(11) Nandy, A.; Adamji, H.; Kastner, D. W.; Vennelakanti, V.; Nazemi, A.; Liu, M.; Kulik, H. J. Using Computational Chemistry To Reveal Nature's Blueprints for Single-Site Catalysis of C–H Activation. *ACS Catal.* **2022**, *12* (15), 9281–9306. DOI: 10.1021/acscatal.2c02096.
(12) Pascanu, V.; González Miera, G.; Inge, A. K.; Martín-Matute, B. Metal-Organic Frameworks as Catalysts for Organic Synthesis: A Critical Perspective. *J. Am. Chem. Soc.* **2019**, *141* (18), 7223–7234. DOI: 10.1021/jacs.9b00733.
(13) Rogge, S. M. J.; Bavykina, A.; Hajek, J.; Garcia, H.; Olivos-Suarez, A. I.; Sepúlveda-Escribano, A.; Vimont, A.; Clet, G.; Bazin, P.; Kapteijn, F.; Daturi, M.; Ramos-Fernandez, E. V.;

Llabrés I Xamena, F. X.; van Speybroeck, V.; Gascon, J. Metal-organic and covalent organic frameworks as single-site catalysts. *Chem. Soc. Rev.* **2017**, *46* (11), 3134–3184. DOI: 10.1039/C7CS00033B.
(14) Herbst, A.; Janiak, C. MOF catalysts in biomass upgrading towards value-added fine chemicals. *CrystEngComm* **2017**, *19* (29), 4092–4117. DOI: 10.1039/c6ce01782g.
(15) Grommet, A. B.; Feller, M.; Klajn, R. Chemical reactivity under nanoconfinement. *Nat. Nanotechnol.* **2020**, *15* (4), 256–271. DOI: 10.1038/s41565-020-0652-2.
(16) Meng, X.; Cui, X.; Rajan, N. P.; Yu, L.; Deng, D.; Bao, X. Direct Methane Conversion under Mild Condition by Thermo-, Electro-, or Photocatalysis. *Chem* **2019**, *5* (9), 2296–2325. DOI: 10.1016/j.chempr.2019.05.008.
(17) Gunay, A.; Theopold, K. H. C-H bond activations by metal oxo compounds. *Chem. Rev.* **2010**, *110* (2), 1060–1081. DOI: 10.1021/cr900269x.
(18) Larson, V. A.; Battistella, B.; Ray, K.; Lehnert, N.; Nam, W. Iron and manganese oxo complexes, oxo wall and beyond. *Nat. Rev. Chem.* **2020**, *4* (8), 404–419. DOI: 10.1038/s41570-020-0197-9.
(19) Hohenberger, J.; Ray, K.; Meyer, K. The biology and chemistry of high-valent iron-oxo and iron-nitrido complexes. *Nat. Commun.* **2012**, *3*, 720. DOI: 10.1038/ncomms1718.
(20) Ray, K.; Pfaff, F. F.; Wang, B.; Nam, W. Status of reactive non-heme metal-oxygen intermediates in chemical and enzymatic reactions. *J. Am. Chem. Soc.* **2014**, *136* (40), 13942–13958. DOI: 10.1021/ja507807v.
(21) Chen, Z.; Yin, G. The reactivity of the active metal oxo and hydroxo intermediates and their implications in oxidations. *Chem. Soc. Rev.* **2015**, *44* (5), 1083–1100. DOI: 10.1039/c4cs00244j.
(22) Osadchii, D. Y.; Olivos-Suarez, A. I.; Szécsényi, Á.; Li, G.; Nasalevich, M. A.; Dugulan, I. A.; Crespo, P. S.; Hensen, E. J. M.; Veber, S. L.; Fedin, M. V.; Sankar, G.; Pidko, E. A.; Gascon, J. Isolated Fe Sites in Metal Organic Frameworks Catalyze the Direct Conversion of Methane to Methanol. *ACS Catal.* **2018**, *8* (6), 5542–5548. DOI: 10.1021/acscatal.8b00505.
(23) Szécsényi, Á.; Khramenkova, E.; Chernyshov, I. Y.; Li, G.; Gascon, J.; Pidko, E. A. Breaking Linear Scaling Relationships with Secondary Interactions in Confined Space: A Case Study of Methane Oxidation by Fe/ZSM-5 Zeolite. *ACS Catal.* **2019**, *9* (10), 9276–9284. DOI: 10.1021/acscatal.9b01914.
(24) Mukherjee, G.; Alili, A.; Barman, P.; Kumar, D.; Sastri, C. V.; Visser, S. P. de. Interplay Between Steric and Electronic Effects: A Joint Spectroscopy and Computational Study of Nonheme Iron(IV)-Oxo Complexes. *Chem. Eur. J.* **2019**, *25* (19), 5086–5098. DOI: 10.1002/chem.201806430.
(25) Snyder, B. E. R.; Bols, M. L.; Rhoda, H. M.; Plessers, D.; Schoonheydt, R. A.; Sels, B. F.; Solomon, E. I. Cage effects control the mechanism of methane hydroxylation in zeolites. *Science* **2021**, *373* (6552), 327–331. DOI: 10.1126/science.abd5803.
(26) Memioglu, O.; Ipek, B. A potential catalyst for continuous methane partial oxidation to methanol using N2O: Cu-SSZ-39. *Chem. Commun.* **2021**, *57* (11), 1364–1367. DOI: 10.1039/d0cc06534j.
(27) Xiao, D. J.; Bloch, E. D.; Mason, J. A.; Queen, W. L.; Hudson, M. R.; Planas, N.; Borycz, J.; Dzubak, A. L.; Verma, P.; Lee, K.; Bonino, F.; Crocellà, V.; Yano, J.; Bordiga, S.; Truhlar, D. G.; Gagliardi, L.; Brown, C. M.; Long, J. R. Oxidation of ethane to ethanol by N2O in a metal-organic framework with coordinatively unsaturated iron(II) sites. *Nat. Chem.* **2014**, *6* (7), 590–595. DOI: 10.1038/nchem.1956.
(28) Sur, A.; Jernigan, N. B.; Powers, D. C. Kinetic Probes of the Origin of Activity in MOF-Based C–H Oxidation Catalysis. *ACS Catal.* **2022**, *12* (7), 3858–3867. DOI: 10.1021/acscatal.1c05415.

(29) Verma, P.; Vogiatzis, K. D.; Planas, N.; Borycz, J.; Xiao, D. J.; Long, J. R.; Gagliardi, L.; Truhlar, D. G. Mechanism of Oxidation of Ethane to Ethanol at Iron(IV)-Oxo Sites in Magnesium-Diluted Fe2(dobdc). *J. Am. Chem. Soc.* **2015**, *137* (17), 5770–5781. DOI: 10.1021/jacs.5b00382.
(30) Gani, T. Z. H.; Kulik, H. J. Understanding and Breaking Scaling Relations in Single-Site Catalysis: Methane to Methanol Conversion by Fe^{IV}=O. *ACS Catal.* **2018**, *8* (2), 975–986. DOI: 10.1021/acscatal.7b03597.
(31) Vitillo, J. G.; Lu, C. C.; Cramer, C. J.; Bhan, A.; Gagliardi, L. Influence of First and Second Coordination Environment on Structural Fe(II) Sites in MIL-101 for C–H Bond Activation in Methane. *ACS Catal.* **2021**, *11* (2), 579–589. DOI: 10.1021/acscatal.0c03906.
(32) Nandy, A.; Duan, C.; Goffinet, C.; Kulik, H. J. New Strategies for Direct Methane-to-Methanol Conversion from Active Learning Exploration of 16 Million Catalysts. *JACS Au* **2022**, *2* (5), 1200–1213. DOI: 10.1021/jacsau.2c00176.
(33) Nandy, A.; Kulik, H. J. Why Conventional Design Rules for C–H Activation Fail for Open-Shell Transition-Metal Catalysts. *ACS Catal.* **2020**, *10* (24), 15033–15047. DOI: 10.1021/acscatal.0c04300.
(34) Jia, H.; Nandy, A.; Liu, M.; Kulik, H. J. Modeling the roles of rigidity and dopants in single-atom methane-to-methanol catalysts. *J. Mater. Chem. A* **2022**, *10* (11), 6193–6203. DOI: 10.1039/D1TA08502F.
(35) Rosen, A. S.; Notestein, J. M.; Snurr, R. Q. Structure–Activity Relationships That Identify Metal–Organic Framework Catalysts for Methane Activation. *ACS Catal.* **2019**, *9* (4), 3576–3587. DOI: 10.1021/acscatal.8b05178.
(36) Barona, M.; Ahn, S.; Morris, W.; Hoover, W.; Notestein, J. M.; Farha, O. K.; Snurr, R. Q. Computational Predictions and Experimental Validation of Alkane Oxidative Dehydrogenation by Fe_2M MOF Nodes. *ACS Catal.* **2020**, *10* (2), 1460–1469. DOI: 10.1021/acscatal.9b03932.
(37) Rosen, A. S.; Notestein, J. M.; Snurr, R. Q. Identifying promising metal-organic frameworks for heterogeneous catalysis via high-throughput periodic density functional theory. *J. Comput. Chem.* **2019**, *40* (12), 1305–1318. DOI: 10.1002/jcc.25787.
(38) Rosen, A. S.; Notestein, J. M.; Snurr, R. Q. High-Valent Metal-Oxo Species at the Nodes of Metal-Triazolate Frameworks: The Effects of Ligand Exchange and Two-State Reactivity for C-H Bond Activation. *Angew. Chem. Int. Ed.* **2020**, *59* (44), 19494–19502. DOI: 10.1002/anie.202004458.
(39) Rosen, A. S.; Notestein, J. M.; Snurr, R. Q. Exploring mechanistic routes for light alkane oxidation with an iron-triazolate metal-organic framework. *Phys. Chem. Chem. Phys.* **2022**, *24* (14), 8129–8141. DOI: 10.1039/d2cp00963c.
(40) Denysenko, D.; Grzywa, M.; Tonigold, M.; Streppel, B.; Krkljus, I.; Hirscher, M.; Mugnaioli, E.; Kolb, U.; Hanss, J.; Volkmer, D. Elucidating gating effects for hydrogen sorption in MFU-4-type triazolate-based metal-organic frameworks featuring different pore sizes. *Chem. Eur. J.* **2011**, *17* (6), 1837–1848. DOI: 10.1002/chem.201001872.
(41) Denysenko, D.; Jelic, J.; Reuter, K.; Volkmer, D. Postsynthetic Metal and Ligand Exchange in MFU-4l: A Screening Approach toward Functional Metal-Organic Frameworks Comprising Single-Site Active Centers. *Chem. Eur. J.* **2015**, *21* (22), 8188–8199. DOI: 10.1002/chem.201406564.
(42) Chen, Z.; Mian, M. R.; Lee, S.-J.; Chen, H.; Zhang, X.; Kirlikovali, K. O.; Shulda, S.; Melix, P.; Rosen, A. S.; Parilla, P. A.; Gennett, T.; Snurr, R. Q.; Islamoglu, T.; Yildirim, T.; Farha, O. K. Fine-Tuning a Robust Metal-Organic Framework toward Enhanced Clean Energy Gas Storage. *J. Am. Chem. Soc.* **2021**, *143* (45), 18838–18843. DOI: 10.1021/jacs.1c08749.
(43) Denysenko, D.; Jelic, J.; Magdysyuk, O. V.; Reuter, K.; Volkmer, D. Elucidating Lewis acidity of metal sites in MFU-4l metal-organic frameworks: N2O and CO2 adsorption in MFU-4l,

CuI-MFU-4l and Li-MFU-4l. *Microporous Mesoporous Mater.* **2015**, *216*, 146–150. DOI: 10.1016/j.micromeso.2015.03.014.
(44) Denysenko, D.; Grzywa, M.; Jelic, J.; Reuter, K.; Volkmer, D. Scorpionate-type coordination in MFU-4l metal-organic frameworks: small-molecule binding and activation upon the thermally activated formation of open metal sites. *Angew. Chem. Int. Ed.* **2014**, *53* (23), 5832–5836. DOI: 10.1002/anie.201310004.
(45) Wright, A. M.; Wu, Z.; Zhang, G.; Mancuso, J. L.; Comito, R. J.; Day, R. W.; Hendon, C. H.; Miller, J. T.; Dincă, M. A Structural Mimic of Carbonic Anhydrase in a Metal-Organic Framework. *Chem* **2018**, *4* (12), 2894–2901. DOI: 10.1016/j.chempr.2018.09.011.
(46) Röß-Ohlenroth, R.; Bredenkötter, B.; Volkmer, D. Organometallic MFU-4l(arge) Metal–Organic Frameworks. *Organometallics* **2019**, *38* (18), 3444–3452. DOI: 10.1021/acs.organomet.9b00297.
(47) Cai, Z.; Bien, C. E.; Liu, Q.; Wade, C. R. Insights into CO_2 Adsorption in M–OH Functionalized MOFs. *Chem. Mater.* **2020**, *32* (10), 4257–4264. DOI: 10.1021/acs.chemmater.0c00746.
(48) Mian, M. R.; Chen, H.; Cao, R.; Kirlikovali, K. O.; Snurr, R. Q.; Islamoglu, T.; Farha, O. K. Insights into Catalytic Hydrolysis of Organophosphonates at M-OH Sites of Azolate-Based Metal Organic Frameworks. *J. Am. Chem. Soc.* **2021**, *143* (26), 9893–9900. DOI: 10.1021/jacs.1c03901.
(49) Szécsényi, Á.; Li, G.; Gascon, J.; Pidko, E. A. Mechanistic Complexity of Methane Oxidation with H_2O_2 by Single-Site Fe/ZSM-5 Catalyst. *ACS Catal.* **2018**, *8* (9), 7961–7972. DOI: 10.1021/acscatal.8b01672.
(50) Kresse; Furthmüller. Efficient iterative schemes for ab initio total-energy calculations using a plane-wave basis set. *Phys. Rev. B Condens. Matter* **1996**, *54* (16), 11169–11186. DOI: 10.1103/physrevb.54.11169.
(51) Blöchl. Projector augmented-wave method. *Phys. Rev. B Condens. Matter* **1994**, *50* (24), 17953–17979. DOI: 10.1103/physrevb.50.17953.
(52) Kresse, G.; Joubert, D. From ultrasoft pseudopotentials to the projector augmented-wave method. *Phys. Rev. B Condens. Matter* **1999**, *59* (3), 1758–1775. DOI: 10.1103/physrevb.59.1758.
(53) Perdew; Burke; Ernzerhof. Generalized Gradient Approximation Made Simple. *Phys. Rev. Lett.* **1996**, *77* (18), 3865–3868. DOI: 10.1103/PhysRevLett.77.3865.
(54) Grimme, S.; Ehrlich, S.; Goerigk, L. Effect of the damping function in dispersion corrected density functional theory. *J. Comput. Chem.* **2011**, *32* (7), 1456–1465. DOI: 10.1002/jcc.21759.
(55) Grimme, S.; Antony, J.; Ehrlich, S.; Krieg, H. A consistent and accurate ab initio parametrization of density functional dispersion correction (DFT-D) for the 94 elements H-Pu. *J. Chem. Phys.* **2010**, *132* (15), 154104. DOI: 10.1063/1.3382344.
(56) Henkelman, G.; Uberuaga, B. P.; Jónsson, H. A climbing image nudged elastic band method for finding saddle points and minimum energy paths. *J. Chem. Phys.* **2000**, *113* (22), 9901–9904. DOI: 10.1063/1.1329672.
(57) Henkelman, G.; Jónsson, H. Improved tangent estimate in the nudged elastic band method for finding minimum energy paths and saddle points. *J. Chem. Phys.* **2000**, *113* (22), 9978–9985. DOI: 10.1063/1.1323224.
(58) Sheppard, D.; Terrell, R.; Henkelman, G. Optimization methods for finding minimum energy paths. *J. Chem. Phys.* **2008**, *128* (13), 134106. DOI: 10.1063/1.2841941.
(59) Heyd, J.; Scuseria, G. E.; Ernzerhof, M. Hybrid functionals based on a screened Coulomb potential. *J. Chem. Phys.* **2003**, *118* (18), 8207–8215. DOI: 10.1063/1.1564060.

(60) Moellmann, J.; Grimme, S. DFT-D3 Study of Some Molecular Crystals. *J. Phys. Chem. C* **2014**, *118* (14), 7615–7621. DOI: 10.1021/jp501237c.
(61) *VASP TST Tools*; Henkelman group. http://theory.cm.utexas.edu/.
(62) Smidstrup, S.; Pedersen, A.; Stokbro, K.; Jónsson, H. Improved initial guess for minimum energy path calculations. *J. Chem. Phys.* **2014**, *140* (21), 214106. DOI: 10.1063/1.4878664.
(63) Hjorth Larsen, A.; Jørgen Mortensen, J.; Blomqvist, J.; Castelli, I. E.; Christensen, R.; Dułak, M.; Friis, J.; Groves, M. N.; Hammer, B.; Hargus, C.; Hermes, E. D.; Jennings, P. C.; Bjerre Jensen, P.; Kermode, J.; Kitchin, J. R.; Leonhard Kolsbjerg, E.; Kubal, J.; Kaasbjerg, K.; Lysgaard, S.; Bergmann Maronsson, J.; Maxson, T.; Olsen, T.; Pastewka, L.; Peterson, A.; Rostgaard, C.; Schiøtz, J.; Schütt, O.; Strange, M.; Thygesen, K. S.; Vegge, T.; Vilhelmsen, L.; Walter, M.; Zeng, Z.; Jacobsen, K. W. The atomic simulation environment—a Python library for working with atoms. *J. Phys.: Condens. Matter* **2017**, *29* (27), 273002. DOI: 10.1088/1361-648x/aa680e.
(64) Xiao, P.; Sheppard, D.; Rogal, J.; Henkelman, G. Solid-state dimer method for calculating solid-solid phase transitions. *J. Chem. Phys.* **2014**, *140* (17), 174104. DOI: 10.1063/1.4873437.
(65) Kästner, J.; Sherwood, P. Superlinearly converging dimer method for transition state search. *J. Chem. Phys.* **2008**, *128* (1), 14106. DOI: 10.1063/1.2815812.
(66) Heyden, A.; Bell, A. T.; Keil, F. J. Efficient methods for finding transition states in chemical reactions: comparison of improved dimer method and partitioned rational function optimization method. *J. Chem. Phys.* **2005**, *123* (22), 224101. DOI: 10.1063/1.2104507.
(67) Henkelman, G.; Jónsson, H. A dimer method for finding saddle points on high dimensional potential surfaces using only first derivatives. *J. Chem. Phys.* **1999**, *111* (15), 7010–7022. DOI: 10.1063/1.480097.
(68) Hunter, J. D. Matplotlib: A 2D Graphics Environment. *Comput. Sci. Eng.* **2007**, *9* (3), 90–95. DOI: 10.1109/MCSE.2007.55.
(69) Humphrey, W.; Dalke, A.; Schulten, K. VMD: Visual molecular dynamics. *J. Mol. Graphics* **1996**, *14* (1), 33–38. DOI: 10.1016/0263-7855(96)00018-5.
(70) Melix, P. *Dataset for "Single-Step Selective Oxidation of Methane by Iron-Oxo Species in the Metal-Organic Framework MFU-4l"*; Zenodo, 2023. DOI: 10.5281/zenodo.6802056.
(71) Melix, P. *Dataset for "Single-Step Selective Oxidation of Methane by Iron-Oxo Species in the Metal-Organic Framework MFU-4l"*; NOMAD, 2023. DOI: 10.17172/NOMAD/2023.05.05-1.
(72) Barona, M.; Gaggioli, C. A.; Gagliardi, L.; Snurr, R. Q. DFT Study on the Catalytic Activity of ALD-Grown Diiron Oxide Nanoclusters for Partial Oxidation of Methane to Methanol. *J. Phys. Chem. A* **2020**, *124* (8), 1580–1592. DOI: 10.1021/acs.jpca.9b11835.
(73) Bols, M. L.; Snyder, B. E. R.; Rhoda, H. M.; Cnudde, P.; Fayad, G.; Schoonheydt, R. A.; van Speybroeck, V.; Solomon, E. I.; Sels, B. F. Coordination and activation of nitrous oxide by iron zeolites. *Nat. Catal.* **2021**, *4* (4), 332–340. DOI: 10.1038/s41929-021-00602-4.
(74) Tolman, W. B. Binding and activation of N_2O at transition-metal centers: recent mechanistic insights. *Angew. Chem. Int. Ed.* **2010**, *49* (6), 1018–1024. DOI: 10.1002/anie.200905364.
(75) Maihom, T.; Choomwattana, S.; Wannakao, S.; Probst, M.; Limtrakul, J. Ethylene Epoxidation with Nitrous Oxide over Fe-BTC Metal-Organic Frameworks: A DFT Study. *ChemPhysChem* **2016**, *17* (21), 3416–3422. DOI: 10.1002/cphc.201600836.
(76) Feldt, M.; Martín-Fernández, C.; Harvey, J. N. Energetics of non-heme iron reactivity: can ab initio calculations provide the right answer? *Phys. Chem. Chem. Phys.* **2020**, *22* (41), 23908–23919. DOI: 10.1039/d0cp04401f.
(77) Phung, Q. M.; Martín-Fernández, C.; Harvey, J. N.; Feldt, M. Ab Initio Calculations for Spin-Gaps of Non-Heme Iron Complexes. *J. Chem. Theory Comput.* **2019**, *15* (8), 4297–4304. DOI: 10.1021/acs.jctc.9b00370.

(78) Feldt, M.; Phung, Q. M.; Pierloot, K.; Mata, R. A.; Harvey, J. N. Limits of Coupled-Cluster Calculations for Non-Heme Iron Complexes. *J. Chem. Theory Comput.* **2019**, *15* (2), 922–937. DOI: 10.1021/acs.jctc.8b00963.
(79) Chen, H.; Lai, W.; Shaik, S. Exchange-Enhanced H-Abstraction Reactivity of High-Valent Nonheme Iron(IV)-Oxo from Coupled Cluster and Density Functional Theories. *J. Phys. Chem. Lett.* **2010**, *1* (10), 1533–1540. DOI: 10.1021/jz100359h.
(80) Chemical Reactivity: Exploring Potential Energy Surfaces. In *A Chemist's Guide to Density Functional Theory*; Koch, W., Holthausen, M. C., Eds.; Wiley, 2001; pp 239–263. DOI: 10.1002/3527600043.ch13.
(81) Cohen, A. J.; Mori-Sánchez, P.; Yang, W. Insights into current limitations of density functional theory. *Science* **2008**, *321* (5890), 792–794. DOI: 10.1126/science.1158722.
(82) Xue, G.; Hont, R. de; Münck, E.; Que, L. Million-fold activation of the Fe(2)(micro-O)(2) diamond core for C-H bond cleavage. *Nat. Chem.* **2010**, *2* (5), 400–405. DOI: 10.1038/nchem.586.
(83) Janardanan, D.; Wang, Y.; Schyman, P.; Que, L.; Shaik, S. The fundamental role of exchange-enhanced reactivity in C-H activation by S=2 oxo iron(IV) complexes. *Angew. Chem. Int. Ed.* **2010**, *49* (19), 3342–3345. DOI: 10.1002/anie.201000004.
(84) Liu, F.; Kulik, H. J. Impact of Approximate DFT Density Delocalization Error on Potential Energy Surfaces in Transition Metal Chemistry. *J. Chem. Theory Comput.* **2020**, *16* (1), 264–277. DOI: 10.1021/acs.jctc.9b00842.
(85) Johnson, R. D. *Computational Chemistry Comparison and Benchmark Database, NIST Standard Reference Database 101*.
(86) Barona, M.; Snurr, R. Q. Exploring the Tunability of Trimetallic MOF Nodes for Partial Oxidation of Methane to Methanol. *ACS Appl. Mater. Interfaces* **2020**, *12* (25), 28217–28231. DOI: 10.1021/acsami.0c06241.
(87) Jasin Arachchige, L.; Dong, A.; Wang, T.; Li, H.; Zhang, X. L.; Wang, F.; Su, H.; Sun, C. Mechanistic Insights into Direct Methane Oxidation to Methanol on Single-Atom Transition-Metal-Modified Graphyne. *ACS Appl. Nano Mater.* **2021**, *4* (11), 12006–12016. DOI: 10.1021/acsanm.1c02564.
(88) Shimoyama, Y.; Kojima, T. Metal-Oxyl Species and Their Possible Roles in Chemical Oxidations. *Inorg. Chem.* **2019**, *58* (15), 9517–9542. DOI: 10.1021/acs.inorgchem.8b03459.
(89) Li, Y.-K.; Müller, F.; Schöllkopf, W.; Asmis, K. R.; Sauer, J. Gas-Phase Mechanism of $O^{\cdot-}$/Ni^{2+}-Mediated Methane Conversion to Formaldehyde. *Angew. Chem. Int. Ed.* **2022**, *61* (29), e202202297. DOI: 10.1002/anie.202202297.
(90) Kovalskii, V. Y.; Ruzankin, S. P.; Snytnikov, V. N.; Zilberberg, I. L. Extremely low barrier activation of methane on spin-polarized ferryl ion $[FeO]^{2+}$ at the four-membered ring of zeolite. *Mol. Catal.* **2022**, *528*, 112468. DOI: 10.1016/j.mcat.2022.112468.
(91) Latimer, A. A.; Kakekhani, A.; Kulkarni, A. R.; Nørskov, J. K. Direct Methane to Methanol: The Selectivity–Conversion Limit and Design Strategies. *ACS Catal.* **2018**, *8* (8), 6894–6907. DOI: 10.1021/acscatal.8b00220.
(92) Teufel, J.; Oh, H.; Hirscher, M.; Wahiduzzaman, M.; Zhechkov, L.; Kuc, A.; Heine, T.; Denysenko, D.; Volkmer, D. MFU-4 - a metal-organic framework for highly effective H_2/D_2 separation. *Adv. Mater.* **2013**, *25* (4), 635–639. DOI: 10.1002/adma.201203383.
(93) Sarkisov, L.; Bueno-Perez, R.; Sutharson, M.; Fairen-Jimenez, D. Materials Informatics with PoreBlazer v4.0 and the CSD MOF Database. *Chem. Mater.* **2020**, *32* (23), 9849–9867. DOI: 10.1021/acs.chemmater.0c03575.

(94) Dudarev, S. L.; Manh, D. N.; Sutton, A. P. Effect of Mott-Hubbard correlations on the electronic structure and structural stability of uranium dioxide. *Philos. Mag. B* **1997**, *75* (5), 613–628. DOI: 10.1080/13642819708202343.
(95) Dudarev, S. L.; Botton, G. A.; Savrasov, S. Y.; Humphreys, C. J.; Sutton, A. P. Electron-energy-loss spectra and the structural stability of nickel oxide: An LSDA+U study. *Phys. Rev. B Condens. Matter* **1998**, *57* (3), 1505–1509. DOI: 10.1103/physrevb.57.1505.
(96) Bajaj, A.; Kulik, H. J. Molecular DFT+U: A Transferable, Low-Cost Approach to Eliminate Delocalization Error. *J. Phys. Chem. Lett.* **2021**, *12* (14), 3633–3640. DOI: 10.1021/acs.jpclett.1c00796.

TOC Graphic